Model for a collimated spin-wave beam generated by a single-layer spin torque nanocontact

M. A. Hoefer,[1,*] T. J. Silva,[1] and M. D. Stiles[2]

[1]*National Institute of Standards and Technology, Boulder, Colorado 80305, USA*
[2]*National Institute of Standards and Technology, Gaithersburg, Maryland 20899, USA*

A model of spin-torque-induced magnetization dynamics based on semiclassical spin diffusion theory for a single-layer nanocontact is presented. The model incorporates effects due to the current-induced Oersted field and predicts the generation of a variety of spatially dependent, coherent, precessional magnetic wave structures. Directionally controllable collimated spin-wave beams, vortex spiral waves, and localized standing waves are found to be excited by the interplay of the Oersted field and the orientation of an applied field. These fields act as a spin-wave "corral" around the nanocontact that controls the propagation of spin waves in certain directions.

PACS number(s): 75.40.Gb, 75.40.Mg, 75.75.+a, 85.75.−d

The flow of sufficiently large dc current through a thin, nanomagnetic structure can give rise to precessional magnetization dynamics at gigahertz frequencies.[1] This remarkable effect has attracted broad interest, both from the standpoint of fundamental physics and in the context of applications. The underlying physics of these spin torque devices is based upon the ability of thin ferromagnetic layers to act as spin filters when current flows through the layers. For spin torque effects to manifest, a source of spin-polarized carriers with a component perpendicular to the magnetization of a layer is required. A typical spin torque multilayer has two primary magnetic layers: a fixed layer that acts as a spin "sieve" that induces a spin accumulation in a nonmagnetic spacer layer and an active layer that can respond dynamically when it absorbs the angular momentum from the accumulated spins. If the active layer has a uniform magnetization, a torque is produced only when the two layers are misaligned.[2]

On the other hand, if the magnetization is not uniform, theory for even a single magnetic layer predicts a nonzero torque with resulting dynamics.[3,4] Single-layer spin torque theory was used to explain differential resistance data in mechanical nanocontact experiments[5] and in lithographically defined nanopillars.[6] Theoretical studies have considered single-layer nanocontact devices,[7] but have not addressed the response of a physically realistic, finite-sized nanocontact with its accompanying Oersted field generated by the dc current flowing through the device.

In general, the total spin accumulation, and hence spin torque, in a magnetic thin film device arises from the lateral and longitudinal diffusion of spins, transverse and parallel to the current direction, respectively.[4] The oft used Slonczewski model of spin torque in trilayers, however, assumes a uniform spin accumulation and incorporates only longitudinal spin diffusion effects.[2]

In this paper, we report a realistic treatment of a single-layer device including lateral and longitudinal spin diffusion, the Oersted field, and a large enough sample geometry to capture novel behavior. Using a novel micromagnetic simulator, we demonstrate unexpected features of the response, including localized standing waves, vortex spiral waves, and, most strikingly, a weakly diffracting collimated beam of spin waves, the direction of which can be steered by changing the direction of an applied magnetic field. The formation of the beam appears to be a novel physical mechanism involving the hybridization of a localized standing wave and a vortex spiral wave. It has been previously shown that spin waves emitted from nanocontact devices can be used to phase-lock two spin torque oscillators.[8] The ability to steer a spin-wave beam with magnetic field could offer a method to selectively control phase locking of multiple spin torque oscillators in an array structure.

The outline of this paper is as follows. First, we describe a two-dimensional (2D) model of spin torque in single-layer nanocontact devices. We then present micromagnetic simulations that demonstrate the wide variety of responses mentioned above. Finally, we explain the results of the simulations using a local formulation of the linear spin-wave dispersion relation above and below the nanocontact, showing how the applied and Oersted fields act as a spin-wave "corral" enabling directional control of anisotropic spin-wave propagation and localized excitations. We also show that this corralling effect is limited neither to this particular model nor the details of spin torque.

The physical system we analyze is pictured in Fig. 1 and is similar to the one theoretically studied in Ref. 4 except that we explicitly treat the finite contact area and Oersted fields. A single ferromagnetic $Ni_{80}Fe_{20}$ (Py) layer is adjacent to two copper (Cu) leads and an insulator. The current flows uniformly in the $-\hat{z}$ direction (electron flow is in the $+\hat{z}$ direction) from a right reservoir located at $z = t_R + t$, through a cylindrical Cu lead of radius r_*, across a Py layer of thickness t at $z = 0$, over to a left reservoir at a distance t_L away
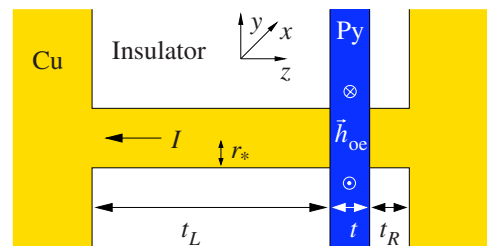

FIG. 1. (Color online) Single-layer nanocontact device schematic. The spatially nonuniform Oersted field $\vec{h}_{oe}$ is generated by the dc current I.

from the magnetic layer ($z=-t_L$). The length t_R is an effective distance over which the current is assumed to maintain quasiunidirectional flow. The magnetic layer is assumed to have infinite extent in the xy directions. When we refer to the region *above* (*below*) the nanocontact, we mean the positive (negative) direction along the y axis.

We calculate the spin accumulation due to current flow through a ferromagnet using the same method described in Ref. 4. We consider the behavior of the spin accumulation in the nonmagnet in response to a nonuniform magnetization $\vec{M}=M_s\vec{u}$, where M_s is the saturation magnetization. As in Ref. 4 we treat the case of small deviations $\vec{u}_\perp$ away from the spatially averaged "equilibrium" direction $\vec{u}_\parallel$. The transverse and longitudinal components of the spin accumulation $\vec{m}$ $=\vec{m}_\perp+\vec{m}_\parallel$, where $\vec{m}_\parallel$ points in the longitudinal direction of the steady-state spin accumulation in the absence of any magnetic inhomogeneity, can be decoupled in this limit. We solve the multipoint boundary value longitudinal problem to find the longitudinal spin accumulation $m_\parallel$ and spin current Q_{zz} for each interface. For deviations at a particular transverse wave vector (k_x,k_y), the transverse spin accumulation is then given in terms of the deviations in the magnetization and the longitudinal solution

$$\mathcal{F}\{\vec{m}_\perp\} = \mathcal{F}\{\vec{u}_\perp\}\frac{\pm Q_{zz}+w_0 m_\parallel}{D\kappa\coth(l'\kappa)+w_0},$$

$$\kappa = (k_x^2+k_y^2+1/l_{sf}^2)^{1/2}, \tag{1}$$

where $\mathcal{F}\{\vec{m}_\perp\}$ and $\mathcal{F}\{\vec{u}_\perp\}$ are the 2D Fourier transforms of the transverse spin accumulation and the magnetization transverse to the average, respectively (+ for right $z=t$ interface and − for left $z=0$ interface). The decoupling of the longitudinal spin accumulation from the transverse spin accumulation is strictly valid only in the limit of small deviations from a uniform magnetization distribution. In our case, the deviations from uniformity are not small, so this treatment should be considered to be a first-order approximation. The distance to the reservoir l' is t_L or t_R for the left and right interfaces, respectively. The spin diffusion length l_{sf} and diffusion constant D are material parameters for Cu; w_0 is the effective interfacial spin absorption rate.

To calculate the transverse spin accumulation in real, polar coordinate (r,ϕ) space, we take the inverse Fourier transform of Eq. (1). Then the expression for $\vec{m}_\perp$, Eq. (A1) (see the Appendix), is the convolution of the magnetization with a weakly singular kernel over the point-contact region. This nonlocal formulation of the transverse spin accumulation can be interpreted as the lateral diffusion of spins interacting with a given magnetization distribution.

We find the quasi-steady-state spin accumulation for a given instantaneous magnetization distribution in the Py layer. This is justified because the ratio of the time scales for the diffusion of electrons to a steady state and for the magnetization dynamics is about 0.001. By formulating the calculation of the inhomogeneous transverse spin accumulation in terms of a simple convolution operation, we have greatly

improved the speed of simulating this effect as compared to directly calculating the coupled magnetization and spin accumulation.[9]

We use the average magnetization direction over the contact $\hat{u}_\parallel$, Eq. (A2), as the orientation of the longitudinal spin accumulation. Physically, this corresponds to the situation where a spin scattered a large number of times from the interface effectively "sees" the average magnetization. The total spin accumulation inside the nanocontact $\vec{m}^*$, Eq. (A3), is then calculated by summing the contributions to the longitudinal and transverse accumulation from each interface. Because an insulator surrounds the Cu leads in our model, the spin accumulation outside the nanocontact is zero.

The dynamical equation for the magnetization is

$$\frac{\partial\vec{u}}{\partial\tau} = -\vec{u}\times\vec{h}_{\mathrm{eff}} - \alpha\vec{u}\times(\vec{u}\times\vec{h}_{\mathrm{eff}}) + \sigma\vec{u}\times(\vec{u}\times\vec{m}^*),$$

$$\vec{h}_{\mathrm{eff}} = \vec{h}_0 - u_z\hat{z} - g(r)\hat{\phi} + \eta\nabla^2\vec{u}, \quad \sigma = \frac{\hbar w_0}{2t\mu_0 M_s^2}. \tag{2}$$

This is a modified 2D Landau-Lifshitz equation in dimensionless form with time normalized by $\gamma\mu_0 M_s$ (γ is the gyromagnetic ratio, μ_0 the permeability of free space). In Eq. (2), space is normalized by r_*, fields and magnetization are normalized by M_s, α is the damping constant, $\eta=D_{\mathrm{ex}}/(\gamma\mu_0 M_s\hbar r_*^2)$ is the coefficient of the exchange term (D_{ex} is the exchange parameter, $\hbar$ Planck's constant divided by 2π), $\vec{h}_0=h_0[\sin(\theta_0)\cos(\psi_0),\sin(\theta_0)\sin(\psi_0),\cos(\theta_0)]$ represents the canted, normalized applied field (θ_0 is measured from the positive z axis, ψ_0 measured counterclockwise from the positive x axis), $-u_z\hat{z}$ is the axial demagnetizing term, and $\vec{h}_J(r,\phi)=-g(r)\hat{\phi}$ is the nonuniform Oersted field due to the current density $J(r)$ defined below. The driving torque is similar to the Slonczewski torque for a trilayer device[2] except that here the torque is nonlocal. We have only considered the leading-order axial component of the dipole field, $-u_z\hat{z}$, which is independent of film thickness t. The calculation of higher-order terms involves integration over the ferromagnetic volume, which greatly complicates the solution of Eq. (2). Higher-order correction terms for such dipole fields have been derived by Arias and Mills.[10] Such correction terms scale as $t\vec{\nabla}\cdot\vec{u}$ and have quantitative significance for large film thicknesses.

The Oersted field is significant in the nanocontact geometry, with a maximum magnitude on the order of 80 kA/m (1000 Oe) for $r_*=40$ nm and $I=21$ mA. Thus, to ignore the Oersted field, as was done in previously presented multilayer simulations,[11] is not an appropriate approximation. We will demonstrate that the Oersted field significantly affects the response of the system. Now we derive the Oersted field for the geometry shown in Fig. 1.

The current density $\vec{J}(r',z')$ in dimensional units (r',z') is modeled as

$$\vec{J}(r',z') = \hat{r}\frac{I}{2\pi D_p r_*}F(r')[H(z'-t-t_R)H(t+t_R+D_p-z')$$
$$-H(-t_L-z')H(z'+t_L+D_p)]$$
$$-\hat{z}\frac{I}{\pi r_*^2}H(r')H(r_*-r')H(t+t_R-z')H(z'+t_L),$$

$$F(r') = \begin{cases} r'/r_*, & 0<r'<r_*, \\ r_*/r', & r_*<r', \end{cases} \qquad H(x) = \begin{cases} 0, & x<0, \\ 1, & x>0. \end{cases}$$

(3)

Two infinite parallel conductor plates of thickness D_p, separated a distance t_R+t+t_L, are connected by a wire of radius r_*. Current flows into the wire from the right plate, through the magnetic layer via a cylinder modeling the point contact, and out of the wire into the left plate. The current flow in the plates is assumed to be in the radial direction only. The coefficient of $\hat{r}$ in (3) models the magnitude of the current density in the plates, assumed uniform in the z direction. Outside of the region where the wire connects to the plates $(r>r_*)$, the current density falls off proportional to $1/r$, whereas inside the region $(r<r_*)$, the current is proportional to r. The current is assumed to flow uniformly down the wire modeled by the coefficient of $\hat{z}$ in (3). This model of current flow conserves the flux of current from the plates to the wire.

We are interested in the value of the Oersted field $\vec{H}_J$, due to the current density (3), in the center of the magnetic layer $z=t/2$.

Using a vector potential representation along with Fourier and Hankel transforms, we solve for the Oersted field in dimensionless units $(r,z)=(r'/r_*,z'/r_*)$ (Ref. 12):

$$\vec{h}_J(r,\phi) = -\hat{\phi}\frac{I}{M_s\pi r_*}\left\{\underbrace{I_1\left(\frac{r}{r_*}\right)}_{\text{infinite wire}} - \underbrace{I_2\left(\frac{r}{r_*}\right)}_{\text{finite wire correction}}\right.$$
$$\left.+\frac{r_*}{M_s D_p}\underbrace{\left[I_3\left(\frac{r}{r_*}\right)+I_4\left(\frac{r}{r_*}\right)\right]}_{\text{conductive plates}}\right\} = -g(r)\hat{\phi}.$$

(4)

The integrals in (4) are

$$I_1(\rho) = \begin{cases} \rho/2, & 0<\rho<1, \\ 1/2\rho, & 1<\rho, \end{cases}$$

$$I_2(\rho) = \int_0^\infty e^{-qa/2}\cosh(qz_*)J_1(q)J_1(q\rho)\frac{1}{q}dq,$$

$$I_3(\rho) = \int_0^\infty e^{-qa/2}(1-e^{-qd})\cosh(qz_*)J_0(q)J_1(q\rho)\frac{1}{q}dq,$$
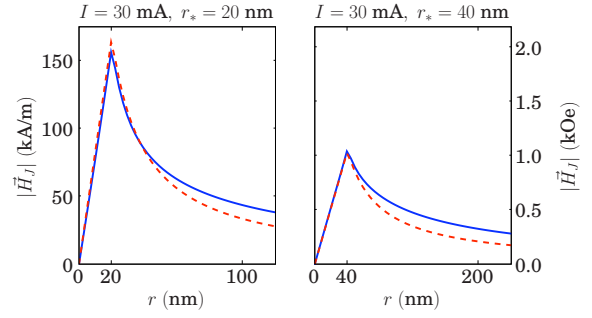

FIG. 2. (Color online) The magnitude of the Oersted magnetic field (4) (solid line) and the Oersted field due to an infinitely long wire with no conductive plates (dashed line).

$$I_4(\rho) = \int_0^\infty e^{-qa/2}(1-e^{-qd})\cosh(qz_*)J_2(q)J_1(q\rho)\frac{1}{q}dq, \quad (5)$$

where $a=(t_R+t+t_L)/r_*$, $d=D_p/r_*$, and $z_*=(t_R-t_L)/2r_*$ are the normalized wire length, conductive plate thickness, and location of the magnetic layer, respectively. J_n are nth-order Bessel functions of the first kind. Note that (4), with $I_2=I_3=I_4\equiv0$, is the result for the magnetic field due to an infinitely long wire of radius r_* with no conductive plates. The magnitude of the Oersted field $h_J(r)=|\vec{h}_J(r,\phi)|$ in (4) depends only on r.

By numerically evaluating the integrals (5), we show $M_s h_J(r)$ for two contact sizes and a fixed current $I=30$ mA in Fig. 2. The fields due to an infinitely long wire with no conductive plates are also shown in Fig. 2 as dashed curves. Equation (4) and the result for an infinite wire agree near the point contact but the decay of the fields is faster for the infinite wire case.

We implemented a numerical method to solve Eq. (2) in polar coordinates (see Appendix). The calculations are rendered tractable by formulating the model in a nonuniform polar coordinate grid, allowing us to compute over a large domain (4.8-μm-diam disk) to avoid boundary spin-wave reflections and with simulation times (3 ns) sufficiently long to ensure that we have determined the true steady-state response. By evolving Eq. (2) in time with a nonuniform initial condition (where $\vec{u}$ is relaxed in the presence of the effective field only), we find that the magnetization settles into a quasiperiodic state due to the competition between the spin accumulation torque and the damping. All excitation frequencies are calculated from the time series of u_y averaged over the nanocontact by use of Fourier methods with a typical resolution of 0.75 GHz. We use the physical parameters listed in Table I of Ref. 4 except $h_0=1.1$, $r_*=40$ nm, $t_R=5$ nm, $t_L=75$ nm, $t=15$ nm, $M_s=800$ kA/m, $D'=0.001$ m^2/s (diffusion rate in Py), $l_{sf}^{FM}=5.5$ nm (spin diffusion length in Py), and $D_p=50$ nm.

Our calculations show a variety of behaviors that depend on the physical parameters including vortex spiral waves [Figs. 3(a) and 4(c)], spin-wave beams [Figs. 3(b) and 4(b)], and localized standing waves [Figs. 3(c) and 4(a)]. The direction of spin-wave propagation in a canted field, $\theta_0>0$, depends on the applied field azimuthal angle ψ_0 where the
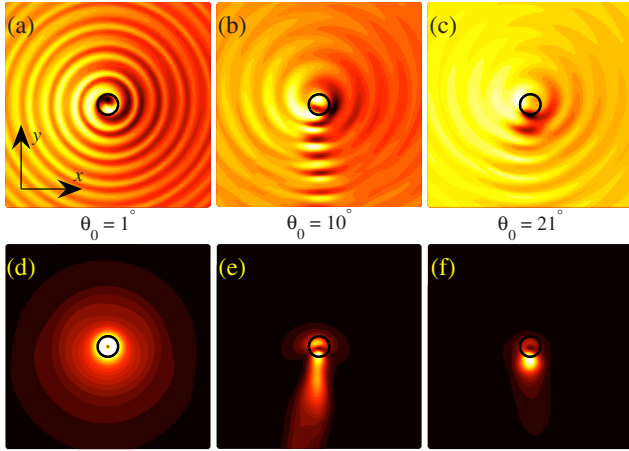
FIG. 3. (Color online) Magnetization (u_y) pattern and energy density of a thin film excited by dc current through a nanocontact with varied applied field canting angle $\theta_0 = 1°$, $10°$, and $21°$ in [(a),(d)], [(b),(e)], [(c),(f)], respectively. All other system parameters are fixed ($I = 29$ mA, $\psi_0 = 0$). The circle in the center represents the boundary of the nanocontact. The plotted domain is a square 10 times the contact diameter per side. Magnitudes in each panel are normalized; positive values are yellow, and negative values are black, with u_y oscillating between approximately ± 0.8, ± 0.6, and ± 0.65 in (a), (b), and (c), respectively. The peak energy density at $r = 10$ in (d), (e), and (f) is, in arbitrary units, 0.74, 1.0, and 0.15 respectively. Note the pinning of the vortex core in (a) and (d). The energy density plot in (e) clearly shows the weak diffraction of the spin-wave beam.

spin-wave angle $\approx \psi_0 - 90°$. The top panels depict the spatial variation of u_y at a specific time, and the lower panels show the energy density for each state. The energy density $E(r, \phi)$ is calculated by taking the time average of the squared magnitude of the magnetization transverse to the average direc-
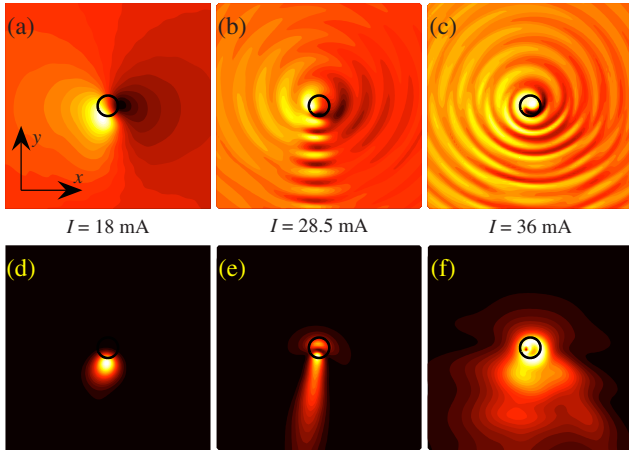

FIG. 4. (Color online) Magnetization (u_y) pattern and energy density of a thin film excited by dc current through a nanocontact with varied dc current $I = 18$, 28.5, and 36 mA in [(a),(d)], [(b),(e)], [(c),(f)], respectively. All other system parameters are fixed ($\theta_0 = 10°$, $\psi_0 = 0°$). u_y oscillates between approximately $[-0.37, 0.34]$, $[-0.53, 0.52]$, and $[-0.97, 0.87]$ in (a), (b), and (c), respectively. The peak energy density at $r = 10$ in (d), (e), and (f) is, in arbitrary units, 0.0051, 0.35, and 1.0, respectively.
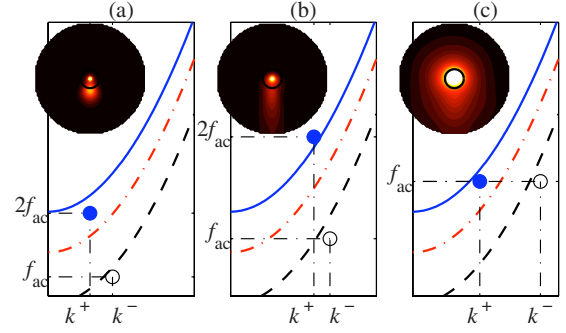

FIG. 5. (Color online) Band structure, excited frequencies, and response energy density for three different driving frequencies: (a) $f_{ac} = 10$ GHz, (b) $f_{ac} = 16$ GHz, and (c) $f_{ac} = 25$ GHz. The solid (open) circles correspond to the numerically determined wave number above (below) the nanocontact and agree with the linear dispersion relation. The FMR frequencies above and below the nanocontact are $f_{FMR}^+ = 20.2$ GHz and $f_{FMR}^- = 5.6$ GHz, respectively. When the drive frequency is in the gap between the upper and lower dispersion relations, the second harmonic $2f_{ac}$ is also excited.

tion, $E(r, \phi) = \langle |\vec{u} \times \langle \vec{u} \rangle|^2 \rangle$, where $\langle f \rangle = \frac{1}{T} \int_{\tau_*}^{\tau_* + T} f \, d\tau$ and τ_* is the time by which the magnetization has settled into a steady, precessional state.

Our choice of a relatively thick Py layer emphasizes the effect of the Oersted field. Larger currents are necessary to excite thicker layers, so that the Oersted fields are larger. Calculations with a thinner Py film still result in localized standing waves, spiral waves, and anisotropic waves, but the collimated beam is more difficult to excite.

The particular response excited can be explained, in part, by appealing to the dispersion relation for a spin wave propagating in a canted uniform field, Eq. (A4). The local fields in the regions above and below the nanocontact (on either side of the nanocontact in the plane of the magnetic film) are of different magnitudes and orientations due to the presence of the nonuniform Oersted field $-g(r)\hat{\phi}$. The Oersted field acts as a "corral" and effectively lifts the spatial degeneracy of the dispersion relation immediately above and below the nanocontact so that, at a given frequency, the spin waves propagate in one direction and evanesce in the other.

The response away from the nanocontact does not strongly depend on the details of spin torque except that the spin torque is localized at the nanocontact. To show this, we solved Eq. (2) with a localized ac applied field $\{\vec{h}_{ac}(r, \phi, t) = h_{ac} \sin(2\pi f_{ac}\tau)\hat{z}, \ r \leq 0.15, \ 0$ elsewhere$\}$, neglecting spin torque. The response and the associated dispersion curves are depicted in Figs. 5(a)–5(c) for $I = 30$ mA, $\theta_0 = 10°$, $\psi_0 = 0°$, and $h_{ac} = 1$. We use the dispersion relation with the local fields evaluated at $r = 1$ to approximate which wave numbers can propagate above (solid blue) and below (dashed black) the nanocontact. The dash-dotted red curve is the far-field dispersion curve where the Oersted field is negligible. The Oersted field creates a gap between the dispersion curves above and below the nanocontact. The type of response excited depends on the driving frequency f_{ac} and its relation to the ferromagnetic resonance (FMR) frequencies [Eq. (A4) with no exchange contribution, $k = 0$] above (f_{FMR}^+), below (f_{FMR}^-), and far away from (f_{FMR}^{far}) the nanocontact. When the
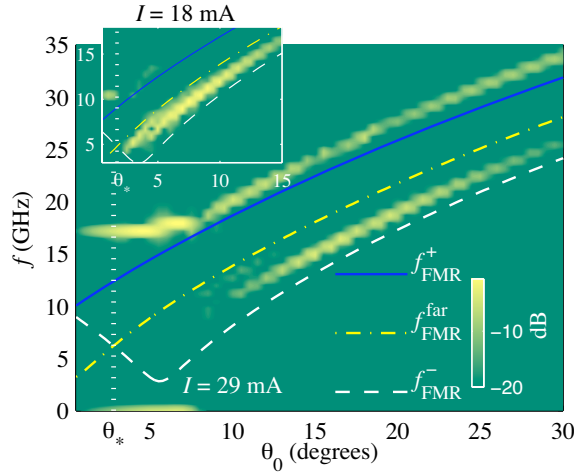
FIG. 6. (Color online) Nanocontact frequency spectrum as a function of applied field polar canting angle θ_0 along with the local FMR frequencies above (f_{FMR}^+), below (f_{FMR}^-), and far away from (f_{FMR}^{far}) the nanocontact. Main plot current: $I=29$ mA. Inset plot current: $I=18$ mA.

driving frequency is between f_{FMR}^- and f_{FMR}^{far}, the excitation is a standing wave [see Fig. 5(a)]. When the driving frequency is between f_{FMR}^{far} and f_{FMR}^+, the excitation forms a spin-wave beam [see Fig. 5(b)]. When the driving frequency is above f_{FMR}^+, the excitation is a nonlocalized propagating wave [see Fig. 5(c)]. This is the "corral" effect; the applied field and the Oersted field act in concert to modify the availability of spin-wave states in close proximity to the nanocontact, depending upon the excitation frequency. In the locations where the Oersted and applied fields add (above the nanocontact), the dispersion relation is shifted upward in frequency, thereby acting as a "fence" to block spin-wave propagation if the excitation frequency is below f_{FMR}^+. Where the Oersted and applied fields cancel, the dispersion relation is shifted downward in frequency, thereby acting as a trap, localizing the spin-wave excitations until the excitation frequency exceeds f_{FMR}^{far}, whereupon the trap is no longer operative and the spin waves are guided downward. The mechanism leading to the standing wave is a linear phenomenon, in contradistinction to previous calculations where nonlinear effects lead to the formation of a localized magnetic excitation in a nanocontact geometry.[13] Even in the presence of a small driving field (e.g., $h_{ac}=0.001$), both the localized wave and the spin-wave beam can be excited, precluding any strong role of nonlinearity in the localization of the response.

We can interpret the different spatial responses in Figs. 3 and 4 by plotting the excitation spectrum as a function of applied field angle (Fig. 6) and applied dc current (Fig. 7). All future local FMR and dispersion curve calculations assume the Oersted field $-g(r)\hat{\phi}$ is evaluated at the radius $r=r_0=1.5$. For currents close to the excitation threshold, the response spectrum has a single-frequency peak that corresponds to vortex spiral waves for small angles and a localized standing wave for larger angles (see the inset of Fig. 6). The lowest available frequency response is excited. For small angles, the localized wave is not available because f_{FMR}^{far} (yellow dash-dotted curve) is less than f_{FMR}^- (white
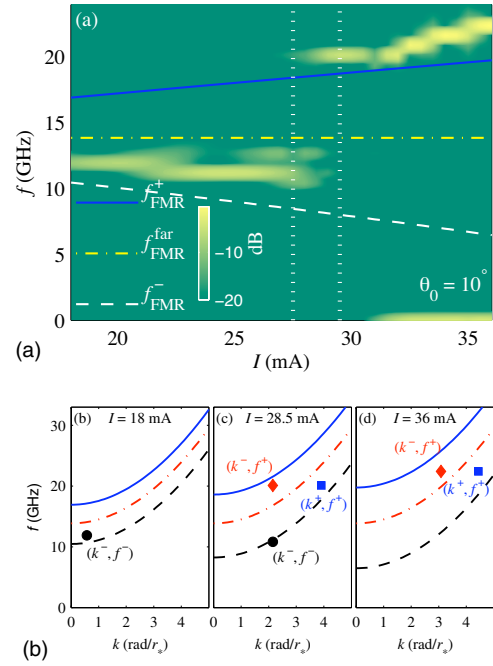

FIG. 7. (Color online) (a) Nanocontact frequency spectrum as a function of dc applied current. (b)–(d) Local dispersion curves evaluated above (blue solid curve), below (black dashed curve), and far from (yellow dash-dotted curve) the nanocontact along with numerically calculated wave numbers and frequencies. (b) The circle is the wave number, frequency pair (k^-,f^-) calculated from the localized wave in Fig. 4(a). (c) The diamond (square) corresponds to the wave number calculated above (below) the nanocontact k^- (k^+) in Fig. 4(b). The two frequencies f^- and f^+ are peaks in the spectrum at $I=28.5$. (d) The diamond and square correspond to the wave number, frequency pairs as discussed for (c), but at the current $I=36$ mA in Fig. 4(c).

dashed curve), so spin waves can propagate to the far field and the vortex spiral wave is excited. Above the critical angle $\theta_*=\sin^{-1}[g(r_0)/(2h_0)]$ where $f_{FMR}^{far}=f_{FMR}^-$ at the radius $r=r_0$, the localized wave with a much lower frequency is excited because its frequency is below f_{FMR}^{far} (see the vertical dotted lines in Fig. 6).

For larger applied currents, nonlinear effects appear to be important. In Fig. 6, the vortex spiral wave is excited for small angles for the same reasons mentioned previously. However, the bifurcation in mode behavior occurs for angles larger than θ_* where, now, there are two distinct frequency peak branches in the spectrum that are not harmonically related. These branches lie just above f_{FMR}^- and f_{FMR}^+ (blue solid curve). In the small-amplitude case (Fig. 6, inset), these branches correspond to the localized standing wave and the vortex spiral wave, respectively. Here, nonlinearity appears to spawn a hybridization of the standing wave and the vortex spiral wave, resulting in the spin-wave beam [see Figs. 3(b) and 4(b)] As the angle is increased, the power associated with each branch changes from being predominantly in the vortex spiral wave branch to being predominantly in the localized wave branch and back again, resulting in a visual change of the energy density as shown in Fig. 3(c) where the standing wave is dominating the response.

This nonlinear hybridization is further investigated in Fig. 7 where the frequency spectrum is plotted as a function of applied current (a) and associated local spin-wave dispersion curves are plotted (b)–(d). For small currents, the localized standing wave is excited due to the corral effect [see Fig. 7(b) and compare with Fig. 5(a)]. For large currents, anisotropic waves are excited because the corral is partially open [see Fig. 7(d)]. For intermediate currents, between the vertical dashed lines in Fig. 7(a), both the localized wave and the spiral wave are excited at the same time, but with different frequencies f^- and f^+. It is only within this current range that we observe the spin-wave beam. There is a *single* wave number associated with these two frequencies, k^-, if the dispersion curve below (above) the contact is associated with the localized standing wave (vortex spiral wave) [see Fig. 7(c)]. The spin-wave beam corresponds to a wave number k^+ associated with the dispersion curve below the contact, but with the larger, vortex spiral wave frequency f^+. These two frequencies and two wave numbers form a triad in the dispersion diagram 7(c). We interpret this behavior in the following way:

$$\left. \begin{array}{c} (f^+,k^-) \ \ \text{spiral} \\ \Uparrow \\ \text{nonlinearity} \\ \| \\ (f^-,k^-) \ \ \text{localized} \end{array} \right\} \underset{\text{hybridization}}{\Rightarrow} (f^+,k^+) \ \ \text{beam}.$$

Given the coarse approximations made in this analysis (linear, 1D behavior and pointwise evaluation of the Oersted field, etc.), the discussion provides a qualitative description of the response selection in single-layer nanocontacts.

The results predicted here for nanocontacts stand in stark contrast to calculations involving nanopillar structures[14] where excitations are confined to a nanomagnet. In the latter case, the Oersted field was shown to effect a small perturbation to the magnetization dynamics. Here, the Oersted field gives rise to the "corral" effect and is fundamental to the formation of magnetic excitations.

We have also performed numerical simulations in trilayer structures (ferromagnet/nonmagnet/ferromagnet), neglecting lateral diffusion and nonlocal effects and using the Slonczewski torque[2] in both our own simulator and in a conventional micromagnetic simulation package (OOMMF) used by a colleague.[15] We find similar qualitative behavior such as the corralling effect and a spin-wave beam. However, we do not observe stable vortex spiral waves and the spatial dependence of the excitations are different. For spin torque magnitudes comparable to that of the single-layer torque discussed in this work, an unphysical, large spin transfer efficiency of 0.7 was required. Theoretical calculations and experimental observations suggest that the spin transfer efficiency is between 0.25 and 0.4.[2,16] Thus, we find that the torque generated by a single layer with nonuniform magnetization can exceed that expected for a uniformly magnetized layer in a trilayer structure, suggesting that inclusion of spin diffusion effects considered here in trilayer calculations may have significant quantitative impact. We note that the semiclassical transport calculations in Ref. 4 used here do not require the use of the spin transfer efficiency, an *ad hoc* parameter, because the spin accumulation is directly calculated in an approximate, but self-consistent manner. We also note that spin diffusion in a trilayer structure has been studied in a self-consistent manner in Ref. 17, but only the linear instability was calculated (i.e., the threshold current for spin-wave excitations) and the calculations were strictly for the case of a uniform current density flowing through an infinitely extended magnetic film without any consideration of boundary conditions. We are currently extending our work to the case of a trilayer nanocontact structure so that the spin accumulation will be calculated in a self-consistent fashion, precluding the need to invoke a spin efficiency factor.

In summary, we have used micromagnetics to predict the generation of a variety of responses in single-layer, nanocontact spin torque devices. A collimated spin-wave beam was observed over a range of currents and applied field angles, with the direction of the beam determined by the applied field azimuthal angle. The interplay of the applied field and the Oersted field act to form a spin-wave corral, effectively trapping excitations under the nanocontact except along the direction where the oscillation frequency matches available propagation states.

APPENDIX

The inverse Fourier transform of Eq. (1) gives

$$\vec{m}_\perp^* \equiv \int_0^{2\pi} \int_0^1 \vec{u}_\perp(r',\phi',\tau)[K_L(R) + K_R(R)]r'\,dr'\,d\phi',$$

$$R(r',\phi';r,\phi) \equiv \sqrt{r^2 + r'^2 - 2rr'\cos(\phi-\phi')}, \quad (A1)$$

where lengths have been normalized by the contact radius r_*, R is the distance between the reference (r',ϕ') and source (r,ϕ) points, τ is time, and we have assumed the thin film limit with $\frac{\partial \vec{u}}{\partial z} = 0$. The kernels K_L and K_R are associated with the left and right interfaces, respectively. Their general expression is

$$K(r) = \frac{a}{r}\int_0^\infty \frac{J_0(k)k\,dk}{\kappa\coth(l\kappa/r) + r/b}, \quad b = D/(w_0 r_*),$$

$$\kappa \equiv [k^2 + (rd)^2]^{1/2}, \quad d = r_*/l_{sf}, \quad l = l'/r_*,$$

$$a = r_*(\pm Q_{zz} + w_0 m_\|)/(2\pi D).$$

A plot of $rK(r)/a$ is shown in Fig. 8 for the typical parameters considered in this work. The average magnetization direction over the contact is
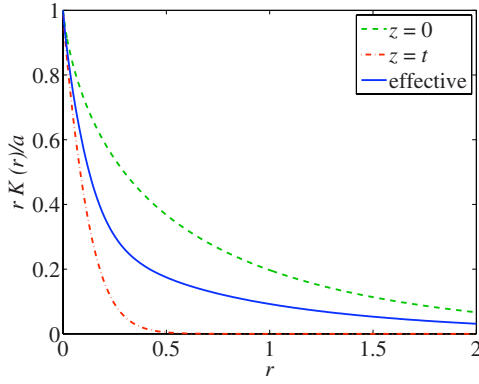
FIG. 8. (Color online) Lateral spin diffusion kernel $rK(r)/a$ multiplied by r to remove the singular behavior and scaled by the constant a to compare the kernel contributions from each interface $[rK_L(r)/a_L$ at $z=0$ (dashed curve) and $rK_R(r)/a_R$ at $z=t$ (dash-dotted curve)] and their combination $(r[K_L(r)+K_R(r)]/(a_L+a_R)$ (solid curve)).

$$\hat{u}_\parallel \equiv \frac{\vec{u}_\parallel}{|\vec{u}_\parallel|}, \quad \vec{u}_\parallel \equiv \frac{1}{\pi}\int_0^{2\pi}\int_0^1 \vec{u}(r',\phi',z,t)r'\,dr'\,d\phi',$$

$$(A2)$$

which we use as the orientation of the longitudinal spin accumulation. The total spin accumulation is

$$\vec{m}^* = \vec{m}^*_\perp + [m_z(0) + m_z(t)]\hat{u}_\parallel, \quad \vec{u}_\perp = \vec{u} - (\vec{u}\cdot\hat{u}_\parallel)\hat{u}_\parallel,$$

$$(A3)$$

where the longitudinal spin accumulation is the sum of the contributions from each interface $z=0$ and $z=t$.

For a uniform applied field of the form $\vec{h}_* = h_*[\sin(\theta_*)\cos(\psi_*), \sin(\theta_*)\sin(\psi_*), \cos(\theta_*)]$, the dispersion relation for exchange spin waves in a thin film is

$$\omega^2 = [\eta k^2 + h_* \cos(\theta_e - \theta_*) - \cos^2(\theta_e)]$$
$$\times [\eta k^2 + h_* \cos(\theta_e - \theta_*) - \cos(2\theta_e)], \quad (A4)$$

where θ_e is the equilibrium magnetization polar angle satisfying $h_* \sin(\theta_e - \theta_*) - \frac{1}{2}\sin(2\theta_e) = 0$.

We briefly discuss the numerical method we have used to solve Eq. (2). The polar coordinate system is a particularly efficient and accurate choice for nanocontact simulations. The discretization we use is nonuniform in radius ("inner" and "outer" grids) and uniform in angle:

$$r_i = q(i - 1/2) \equiv \frac{1}{2}(dr_{in} + dr_{out})(i - 1/2)$$

$$+ \frac{1}{2}(-dr_{in} + dr_{out})w \ln$$

$$\times \left[\cosh\left(\frac{\hat{i} - i + 1/2}{w}\right)\Big/\cosh\left(\frac{\hat{i}}{w}\right)\right],$$

$$\phi_j = -\pi + (j-1)d\phi, \quad d\phi = \frac{2\pi}{M},$$

$$i = 1, \dots, N, \quad j = 1, \dots, M,$$

where $\hat{i}$ and w are parameters determining the location and width of the smooth change from the fine inner-grid spacing dr_{in} to the coarser outer-grid spacing dr_{out}. The advantage of this discretization is that we can solve on a uniform computational grid $(i-1/2, \phi_j)$, but the physical grid (r_i, ϕ_j) is clustered in and around the point contact where the interesting dynamics occur. The outer grid supports the propagation of spin waves of the appropriate wavelength away from the point contact. We choose a domain large enough $0 < r < L$, $L \gg 1$, so that wave reflections off the boundary do not affect the solution inside the point contact. For comparison, our simulations on a circular domain with diameter $2Lr_* = 2 \times 100 \times 40$ nm$= 8$ μm involve $MN = 32 \times 502 = 16\,064$ grid points. A nonuniform grid in the Cartesian coordinate system covering the same domain would involve $4N^2 = 1 \times 10^6$ grid points while a uniform grid would require 16×10^6 grid points.

The boundary condition for Eq. (2) is the Neumann condition $\frac{\partial\vec{u}}{\partial r}(r=L, \phi, \tau)=0$. We approximate radial derivatives using sixth-order finite differences and the angular derivative $\vec{u}_{\phi\phi}$ is calculated using a pseudospectral, fast Fourier transform method. An explicit Runge-Kutta fourth-order time-stepping method is used to advance Eq. (2) forward in time. To avoid severe time-step restrictions due to the small grid spacing near the origin, we apply a smooth, radial grid-dependent angular mask $g_i(k)$ at every time step that filters out numerically induced small wavelengths near the origin.[18] The mask applied to positive angular mode k at the radial grid point r_i takes the form

$$g_i(k) = \frac{1}{2} + \frac{1}{2}\tanh\left(\frac{k_i - k}{\Delta k}\right), \quad k_i = \frac{k_0 r_i}{2r_1},$$

and is evenly extended to negative k values.

Numerical parameters we use are $dr_{in} = 0.05$, $dr_{out} = 0.25$, $w = 10$ $\hat{i} = 126$, $M = 32$, and $N = 342$ for Figs. 6 and 7; $\hat{i} = 273$, $M = 64$, and $N = 455$ for Figs. 3 and 4; $L = 60$; $k_0 = 3$ (wave number cutoff in angular mask at $r = r_1$); and $\Delta k = 1$ (width of wave number cutoff in angular mask). We find no significant change in the results for more accurate grids and filtering parameters.

The convolution $m^*_\perp\{\vec{u}_\perp\}$ in Eq. (A1) is evaluated on the computational grid using Simpson's rule in both the angular and radial directions. To deal with the removable singularity when $R=0$ in Eq. (A1), we subtract off the small-R behavior:

$$K(R) = af(R)/R \sim a[1/R + \ln(R)/b + G] + o(1), \quad R \ll 1,$$

where G is a constant. The resulting integral, at one interface, which we evaluate numerically, is

$$\vec{m}_\perp = \int_0^{2\pi} \int_0^1 \frac{af(R)\vec{u}'_\perp - a[1 + R\ln(R)/b]\vec{u}_\perp}{R} r' dr' d\phi'$$

$$+ a4E(r^2)\vec{u}_\perp + \frac{a}{b}\vec{u}_\perp \int_0^{2\pi} \int_0^1 \ln(R)r' dr',$$

$$\vec{u}'_\perp \equiv \vec{u}_\perp(r', \phi', \tau), \quad \vec{u}_\perp \equiv \vec{u}_\perp(r, \phi, \tau),$$

where $4E(r^2) = \int_0^{2\pi}\int_0^1 r'/R \, dr' \, d\phi'$ and E is the complete elliptic integral of the second kind.

*hoefer@boulder.nist.gov

[1] S. I. Kiselev, J. C. Sankey, I. N. Krivotorov, N. C. Emley, R. J. Schoelkopf, R. A. Buhrman, and D. C. Ralph, Nature (London) **425**, 380 (2003); W. H. Rippard, M. R. Pufall, S. Kaka, S. E. Russek, and T. J. Silva, Phys. Rev. Lett. **92**, 027201 (2004).

[2] J. C. Slonczewski, J. Magn. Magn. Mater. **159**, L1 (1996).

[3] M. L. Polianski and P. W. Brouwer, Phys. Rev. Lett. **92**, 026602 (2004).

[4] M. D. Stiles, J. Xiao, and A. Zangwill, Phys. Rev. B **69**, 054408 (2004).

[5] Y. Ji, C. L. Chien, and M. D. Stiles, Phys. Rev. Lett. **90**, 106601 (2003).

[6] B. Ozyilmaz, A. D. Kent, J. Z. Sun, M. J. Rooks, and R. H. Koch, Phys. Rev. Lett. **93**, 176604 (2004); B. Ozyilmaz and A. D. Kent, Appl. Phys. Lett. **88**, 162506 (2006).

[7] S. Adam, M. L. Polianski, and P. W. Brouwer, Phys. Rev. B **73**, 024425 (2006); H. Xi, Y. Yang, J. Ouyang, Y. Shi, and K. Gao, *ibid.* **75**, 174411 (2007).

[8] S. Kaka, M. R. Pufall, W. h. Rippard, T. J. Silva, S. E. Russek, and J. A. Katine, Nature (London) **437**, 389 (2005); F. B. Mancoff, N. D. Rizzo, B. N. Engel, and S. Tehrani, *ibid.* **437**, 393 (2005); M. R. Pufall, W. H. Rippard, S. E. Russek, S. Kaka, and J. A. Katine, Phys. Rev. Lett. **97**, 087206 (2006).

[9] C. J. Garcia-Cervera and X. Wang, J. Comput. Phys. **224**, 699 (2007).

[10] R. E. Arias and D. L. Mills, Phys. Rev. B **75**, 214404 (2007).

[11] M. A. Hoefer, M. J. Ablowitz, B. Ilan, M. R. Pufall, and T. J. Silva, Phys. Rev. Lett. **95**, 267206 (2005); D. V. Berkov and N. L. Gorn, J. Appl. Phys. **99**, 08Q701 (2006); G. Consolo, B. Azzerboni, G. Gerhart, G. A. Melkov, V. Tiberkevich, and A. N. Slavin, Phys. Rev. B **76**, 144410 (2007).

[12] M. A. Hoefer, Ph.D. thesis, University of Colorado, 2006.

[13] A. Slavin and V. Tiberkevich, Phys. Rev. Lett. **95**, 237201 (2005).

[14] I. N. Krivorotov, D. V. Berkov, N. L. Gorn, N. C. Emley, J. C. Sankey, D. C. Ralph, and R. A. Buhrman, Phys. Rev. B **76**, 024418 (2007).

[15] S. E. Russek (unpublished).

[16] M. R. Pufall, W. H. Rippard, and T. J. Silva, Appl. Phys. Lett. **83**, 323 (2003).

[17] A. Brataas, Y. Tserkovnyak, and G. E. W. Bauer, Phys. Rev. B **73**, 014408 (2006).

[18] B. Fornberg, SIAM J. Sci. Comput. **16**, 1071 (1995).